UNIVERSITÀ DEGLI STUDI DI MILANO

DOCTORAL PROGRAM IN CLINICAL RESEARCH

XXXVIII cycle

DEPARTMENT OF BIOMEDICAL, SURGICAL, AND DENTAL SCIENCES

DTI-ALPS REFLECTS WHITE MATTER DIFFUSION ANISOTROPY AND MICROSTRUCTURAL HETEROGENEITY RATHER THAN GLYMPHATIC FLOW: INSIGHTS FROM MULTI-MODAL MRI

Doctoral Project of:

Luca Sacchi MD

Matr. n. R13981

Tutor:

Chiar.ma Prof.ssa Daniela Galimberti

Director of the PhD program:

Chiar.mo Prof. Massimo Del Fabbro

2024-2025

SUMMARY

1. ABSTRACT

The glymphatic system plays a critical role in the clearance of metabolic waste and pathological proteins such as amyloid-β and tau from the brain, and its dysfunction has been increasingly implicated in the pathogenesis of neurodegenerative diseases, making its in vivo characterization a major research priority. The diffusion tensor imaging–analysis along the perivascular space (DTI-ALPS) has been widely adopted as a putative non-invasive MRI biomarker of glymphatic flow. However, the biological specificity of the DTI-ALPS index remains unclear, and recent evidence has raised concerns that it may primarily reflect white-matter (WM) microstructure rather than perivascular fluid transport. In this study, we sought to clarify the determinants of DTI-ALPS and to assess whether this metric primarily reflects WM microstructural damage rather than glymphatic activity.

A total of 100 participants were recruited from individuals referred to the Neurodegenerative Diseases Unit of the Fondazione IRCCS Ca' Granda Ospedale Maggiore Policlinico in Milan (Italy) for suspected dementia. All the participants underwent the same 3T MRI protocol comprising high-resolution T1-weighted and FLAIR imaging, double-shell diffusion-weighted imaging (b=1000 and 2000 s/mm²), and multi-echo gradient-echo sequences for quantitative susceptibility mapping. Within standard centrum semiovale regions of interest, we computed DTI-ALPS together with fractional anisotropy (FA), mean diffusivity (MD), mode of anisotropy (MA), and neurite orientation and density imaging (NODDI) metrics, including the orientation dispersion index (ODI), neurite density index (NDI), and isotropic volume fraction (FISO). We also computed the T1/FLAIR signal ratio and the diamagnetic component of susceptibility (DCS) derived from DECOMPOSE within the same ROIs, as complimentary structural metrics of WM damage.

Lower DTI-ALPS values were associated with higher FA and MD (|r|=0.40–0.60), with stronger effects observed at b=2000 than at b=1000. The DTI-ALPS index correlated strongly and inversely with MA (r=–0.84 at b=1000; r=–0.86 at b=2000) and positively with ODI (r=0.73), and both metrics remained strong independent predictors after correction for age and sex. Moderate associations were observed with structural markers—direct with the T1/FLAIR ratio (r 0.33) and inverse with DCS standard deviation (r -0.50) —consistent with altered myelin integrity and increased microstructural heterogeneity. Exploratory factor analysis demonstrated that DTI-ALPS did not form a separate latent component but clustered with MA and ODI, indicating shared variance related to axonal geometry rather than to perivascular flow.

Collectively, these findings demonstrate that DTI-ALPS predominantly reflects WM architecture—specifically, loss of crossing fibers, increased diffusion coherence, and reduced orientation dispersion—rather than the dynamics of glymphatic transport. Although DTI-ALPS may still capture secondary effects of glymphatic impairment arising from WM injury, the present results suggest that it cannot be considered a direct biomarker of glymphatic function. Its use as a surrogate measure of glymphatic flow should therefore be approached with caution and re-evaluated through direct validation against intrathecal contrast-enhanced MRI or other physiological reference methods.

2. INTRODUCTION

The glymphatic system (GS) is a brain-wide perivascular network that mediates the flow and clearance of cerebrospinal fluid (CSF) and solutes through the brain parenchyma, facilitated by aquaporin-4 channels on astrocytic endfeet [1–3].

Its description in 2012[4] reshaped our understanding of cerebral fluid dynamics and was later complemented by the (re)discovery of meningeal lymphatic vessels in the dura[5,6], as well as the identification of direct connections linking the subarachnoid space with dural perisinus compartments[7], and the latter with the bone marrow within the thecal bone[8–10].

Together, these findings established the glymphatic–lymphatic model, with known roles in metabolic waste clearance[11] and immune surveillance of the brain[3,12]. Dysfunction of this system has been implicated in neurodegeneration, both through impaired clearance of pathological proteins such as amyloid-β[4] and tau[13,14], and through altered immune responses to neuropathology[12], underscoring its potential as a target for pharmacological intervention. Consequently, the in vivo visualization and assessment of glymphatic flow in humans have become a prominent focus of research.

Although the expression *study of the glymphatic system* has often been applied to approaches aimed at broadly characterizing CSF dynamics—from its production in the choroid plexus, to its movement along major subarachnoid vessels, and its drainage into meningeal lymphatic vessels—the core of the GS lies in the parenchymal passage of fluid, which has also proven to be the most elusive to measure.

Contrast-enhanced magnetic resonance imaging (CE-MRI) following intrathecal gadolinium administration is regarded as the gold standard for in vivo evaluation of the GS[15], as it enables quantification of CSF flow within the brain parenchyma under both physiological[16] and pathological conditions[17]. However, this technique is invasive, carries a risk of adverse effects and gadolinium-related toxicity, and requires prolonged serial MRI acquisitions over several hours or even days.

CE-MRI after intravenous gadolinium administration has been proposed as a less invasive alternative[18]. However, this approach remains poorly standardized[19], and its interpretation is complicated by the fact that contrast leakage from the vasculature into the central nervous system can occur through multiple pathways with distinct concentration–time profiles[20]. Moreover, the high intravascular gadolinium signal often obscures subtler extravascular changes, further complicating image analysis[20].

As a result, recent studies have increasingly focused on finding non-invasive biomarkers of GS function. Among these, the diffusion tensor imaging–analysis along the perivascular space (DTI-ALPS)[21] has gained popularity, mainly because of its technical simplicity. This

method was developed to measure water diffusion along the perivascular spaces of medullary veins while reducing the confounding effect of white matter (WM) fiber orientation. Since its introduction in 2017, DTI-ALPS has been widely used, especially in research on neurodegenerative diseases[22–30]. In these studies, lower DTI-ALPS values have been linked cross-sectionally to poorer cognitive performance and greater disability, and longitudinally to faster clinical decline over time, particularly in Alzheimer's disease (AD). These findings have been interpreted as supporting evidence that glymphatic dysfunction contributes to the pathogenesis of neurodegenerative diseases.

More recently, however, the actual sensitivity of this metric to glymphatic flow has been questioned[31,32]. Emerging data suggest that the DTI-ALPS index may be influenced by WM microstructural properties and damage[33–35], also considering its derivation from an anatomically complex region with numerous crossing fibers[36,37]. This may be particularly relevant in the context of neurodegenerative dementias. Although traditionally viewed as disorders of the grey matter, these conditions are characterize by early and promient WM degeneration and demyelination[38,39]. In AD, for instance, WM damage is widespread[40] and appears to follow a "retrogenesis" model, in which degenerative processes mirror the reverse sequence of developmental myelination[41,42].

Diffusion-weighted imaging (DWI) is arguably the most sensitive technique to WM microstructural alteration. Most commonly, diffusion-related parameters are derived using the diffusion tensor imaging (DTI) model. Among DTI–derived metrics, fractional anisotropy (FA) and mean diffusivity (MD) have been widely used to study WM changes in neurodegenerative diseases, typically showing widespread decrease of FA and MD compatible with degeneration of WM tracts[40]. The mode of anisotropy (MA), a less commonly used DTI metric, complements FA by distinguishing between linear and planar diffusion patterns[43]. Whereas FA reflects the overall degree of diffusion anisotropy, MA characterizes the tensor shape and provides insight into local fiber geometry, particularly in regions of complex architecture[44].

DTI is a widely acknowledged model that, however, suffers from several limitations[45], particularly the partial volume effect of extracellular free water. The Neurite Orientation Dispersion and Density Imaging (NODDI)[46] extends conventional DTI by modeling the diffusion signal into three biologically meaningful compartments: (i) the intra-neurite compartment, characterized by restricted diffusion within neurites; (ii) the extra-neurite compartment, reflecting hindered diffusion in the surrounding space; and (iii) the isotropic compartment, representing free water diffusion. Its key parameters—the neurite density index (NDI) and the orientation dispersion index (ODI)—quantify axonal density and angular variability of neurite orientation, respectively. Together, NDI and ODI provide more specific and interpretable insights into microstructural alterations, as they disentangle

changes in neurite density and orientation dispersion that can produce similar effects on FA[47].

Structural MRI has been shown to provide complimentary information to DWI imaging in the assessment of WM degeneration[48], with the advantage of ease of accessibility. In particular, two imaging indices originally developed in the context of neuroinflammatory and demyelinating diseases have been proposed as structural markers of WM damage with possible applications in neurodegenerative diseases. The first is the ratio of T1- to T2-weighted[49] or fluid-attenuated inversion recovery (FLAIR) signal intensity[50,51], which has been shown to correlate with WM degeneration and poorer cognitive performance in AD and other neurodegenerative conditions[52,53].

The second is quantitative susceptibility mapping (QSM), an MRI technique that non-invasively quantifies tissue magnetic susceptibility, primarily reflecting contributions from iron and myelin[54]. However, conventional QSM does not resolve sub-voxel variations in susceptibility and opposing diamagnetic (myelin-related) and paramagnetic (iron-related) sources may partially cancel each other, leading to artificially low or near-zero total values. To overcome this limitation, advanced algorithms have been developed to separate the diamagnetic (DCS) and paramagnetic (PCS) components of the QSM signal, enabling more specific assessment of myelin and iron content. This approach has shown promise as a potential tool for tracking pathological neurodegeneration across different brain regions and tissue types[55,56].

Against this background, in this study we sought to clarify the biological specificity of the DTI-ALPS index by assessing the potential confounding influence of WM microstructural alterations in the context of neurodegenerative disease. We examined a cohort of patients with suspected dementia, enriched for AD cases, and evaluated associations between DTI-ALPS and complementary MRI markers of WM damage within the same regions of interest (ROIs) used for DTI-ALPS computation. Specifically, we first examined correlations with DTI metrics at b=1000 and b=2000 to assess how their relationship with DTI-ALPS changes at higher diffusion weightings, which progressively suppress the contribution of freely diffusing water[57]. Then, we looked for a better explanation of these results with NODDI-derived indices reflecting neurite density, orientation dispersion and extracellular free water. Lastly, we compared DTI-ALPS with structural MRI markers of WM damage. This multimodal approach aimed to disentangle whether the DTI-ALPS index primarily reflects WM microstructural damage rather than glymphatic flow.

3. MATERIALS AND METHODS

3.1 Study participants

A total of 100 participants were recruited from individuals referred to the Neurodegenerative Diseases Unit of the Fondazione IRCCS Ca' Granda Ospedale Maggiore Policlinico in Milan (Italy) for suspected dementia.

To be eligible for inclusion, subjects were required to have undergone the same MRI protocol on a 3T Philips Achieva dStream scanner (Philips Healthcare, Best, The Netherlands). The MRI protocol included:

i) a volumetric high-resolution T1-weighted Spoiled Gradient Echo (T1-SPGR);

ii) a volumetric FLAIR;

iii) a double-shell (b = 1000 and b = 2000) DWI (single-shot spin-echo echo-planar imaging) sequence acquired with opposite phase-encoding directions (posterior–anterior and anterior–posterior); and

iv) a 3D multi-echo gradient echo (GRE) sequence suitable for QSM. Detailed MRI acquisition parameters are provided in **Table 1**.

Table 1. **MRI protocol**

Sequence / Protocol	3D-T1	3D-FLAIR	DWI (EPI)	QSM (multi-echo GRE)
Plane	Sagittal	Sagittal	Axial	Axial
TR (ms)	8.2	5000	8400	40
TE (ms)	3.8	300	85	5.4-36.6
ΔTE (ms)	-	-	-	5.2
Echoes	1	1	1	7
TI (ms)	-	1700	-	-
Slice thickness (mm)	1	1	2.5	1
Slice spacing (mm)	1	1	0	0
Flip angle (¬∞)	8	120	90	18
Matrix	240x240	240x240	96x96	224x224
b-values	-	-	1000/2000	-
Enchoding directions	-	-	32/32	-
Phase encoding (main)	-	-	PA	-

Abbreviatons: *FLAIR*: fluid-attenuated inversion recovery; *DWI*: diffusion-weighted imaging; *EPI*: echo-planar imaging; *QSM*: quantitative susceptibility mapping; *GRE*: gradient echo; *TR*: repetition time; *TE*: echo time; *TI*: inversion time; *PA*; postero-anterior

At baseline, all participants underwent a standardized diagnostic assessment, including detailed medical history, general and neurological examination, comprehensive neuropsychological testing and mini-mental state examination (MMSE), MRI, and—when clinically indicated—CSF analysis and/or ^{18}F-fluorodeoxyglucose positron emission tomography (FDG-PET) and/or amyloid-PET.

Participants underwent clinical follow-up every six months for at least 12 months. Based on longitudinal evaluation, individuals were classified as having a progressive neurodegenerative disorder (either of AD[58,59] or non-AD type[60–64]) or a non-degenerative condition, defined as stable mild cognitive impairment (sMCI), when no evidence of disease progression or longitudinal cognitive decline was observed.

Cognitively unimpaired (CU) participants presented with subjective cognitive complaints but exhibited no measurable impairment at formal neuropsychological testing nor evidence of an underlying neurodegenerative process after an extensive diagnostic work-up.

Exclusion criteria included: (i) MRI evidence of significant cerebrovascular pathology, cerebral amyloid angiopathy, or intracranial mass lesions; (ii) diagnosis of normal pressure hydrocephalus; and (iii) presence of severe motion artifacts compromising image quality.

3.2. DWI preprocessing, DTI metrics extraction and DTI-ALPS analysis

The DTI-ALPS index was automatically computed using the FSL-based pipeline developed by Liu et al[65].

Briefly, DWI were preprocessed in FSL[66,67]. After DICOM-to-NIfTI conversion, images were corrected for susceptibility-induced field inhomogeneities and subject motion using topup[68] and eddy[69]. A brain mask was then generated from the averaged b0 volumes using BET[70].

Diffusion tensor fitting was performed with dtifit considering the b=1000 and b=2000 s/mm² shells separately. This produced voxel-wise maps of FA, MD, and full diffusion tensors for each b-value.

FA maps were normalized to the high-resolution FMRIB58_FA standard space image using linear and non-linear registrations (FLIRT and FNIRT)[71], and tensors were transformed into the same space with vector correction. Directional tensor components (Dxx, Dyy, Dzz) were extracted, and all indices were computed within default ROIs corresponding to 2.5-mm-radius spheres located in projection and association fibers of both hemispheres, as defined in the Johns Hopkins University (JHU) atlas.

The DTI-ALPS index was calculated separately for each b-value (referred to as DTI-$ALPS_{1000}$ and DTI-$ALPS_{2000}$ throughout the text) as the ratio between diffusivity along the x-axis and the mean diffusivity along the orthogonal (y and z) axes in the 4 ROIs, yielding

a global value. Mean FA and MD were also computed across the four ROIs for both b-values (FA_{1000}, FA_{2000}, MD_{1000}, and MD_{2000}).

Additionally, MA was calculated following the formulation described by Ennis and Kindlmann to obtain mean global MA across the four ROIs for both diffusion weightings (MA_{1000} and MA_{2000})[43]. Beyond the magnitude of anisotropy captured by FA, the MA describes the tensor's geometric configuration, varying from linear (MA ≈ +1) to planar (MA ≈ –1) and isotropic (MA ≈ 0), and reflects the relative distribution of the diffusion eigenvalues (**Figure 1**).

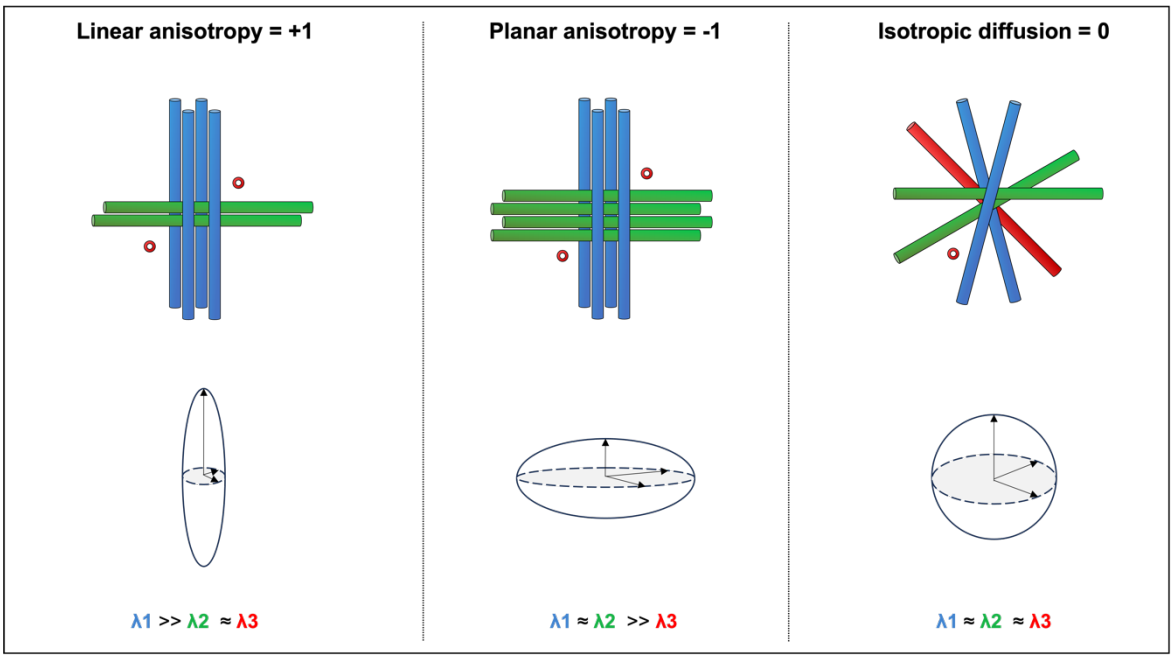

Figure 1. Schematic representation of fiber geometry and corresponding mode of anisotropy (MA). Coherently aligned fibers produce a prolate (linear) tensor shape with high MA (*left*). Crossing fibers with comparable orientations generate an oblate (planar) tensor with reduced MA (*center*). Disorganized or heterogeneous fiber orientations result in an isotropic (spherical) tensor, with MA values approaching zero (*right)*.

3.3 T1 and FLAIR images preprocessing and T1/FLAIR ratio calculation

T1/FLAIR ratio maps were processed following a multistep pipeline available at https://github.com/treanus/KUL_NIS, as referenced in Cappelle[51]. Briefly, intensity nonuniformities due to field inhomogeneity were corrected using the N4 bias field correction algorithm implemented in ANTs[72]. The bias-corrected FLAIR images were then rigidly coregistered to the corresponding T1 volumes using antsRegistration.

T1 images were subsequently nonlinearly normalized to the MNI152 (ICBM) standard space, producing forward and inverse deformation fields.

To improve inter-subject comparability, intensity calibration was carried out within brain masks of both the subject and the MNI template, as implemented in the calib-nonlin3 procedure of the original code. During this step, the intensity histogram of each subject was nonlinearly adjusted to match that of the reference template, in order to standardize intensity distribution across subjects and minimize variations related to receiver gain or acquisition conditions. Calibrated T1 and FLAIR images were then combined voxel-wise to compute T1/FLAIR ratio maps. These ratio maps were spatially normalized to MNI space using the forward deformation fields derived from T1 normalization, and the mean T1/FLAIR ratio was extracted within the four DTI-ALPS ROIs (referred to as $T1/FLAIR_{ratio}$).

3.4 DCS map calculation

DCS maps were derived using the DECOMPOSE algorithm developed by Chen et al.[73]. In this method, QSM reconstructed at each echo is used to fit a three-pool signal model representing paramagnetic (primarily iron-related), diamagnetic (primarily myelin-related), and magnetically neutral tissue compartments. Through this framework, the relative contributions of each magnetic source to the total susceptibility can be estimated voxel-wise.

For the DECOMPOSE reconstruction, only the first five echoes were used, as later echoes typically exhibited lower signal-to-noise ratio and greater phase instability[55]. DCS values were kept in their native units without normalization to a reference region, avoiding assumptions about brain areas presumed to be spared from neurodegenerative changes[54].

The resulting DCS maps were then coregistered to the corresponding native T1-weighted images and normalized to the MNI152 (ICBM) standard space with the same modalities applied for the $T1/FLAIR_{ratio}$ calculation. All maps were visually inspected to confirm image quality, artifact suppression, and spatial correspondence prior to inclusion in subsequent analyses.

Subsequently, a histogram-based characterization of DCS values was performed. For each participant, the mean (DCS_{mean}), median (DCS_{med}), standard deviation (DCS_{std}), kurtosis (DCS_{kurt}), skewness (DCS_{skew}), and the 10th (DCS_{p10}), 25th (DCS_{p25}), 75th (DCS_{p75}), and 90th (DCS_{p90}) percentiles were extracted by averaging values within the four DTI-ALPS ROIs[74].

3.5 NODDI metrics extraction

Microstructural diffusion parameters were estimated using the NODDI model[46] implemented within the AMICO (Accelerated Microstructure Imaging via Convex

Optimization) framework[75]. The AMICO pipeline was applied to DWI that had been preprocessed for eddy current, motion, and susceptibility-induced distortion correction.

Within the AMICO framework, the NODDI model was fitted assuming three diffusion compartments: (i) an intra-neurite compartment representing restricted diffusion within neurites, (ii) an extra-neurite compartment modeling hindered diffusion in the surrounding tissue, and (iii) an isotropic compartment reflecting free water diffusion.

For each subject, the following parametric maps were generated: intracellular volume fraction, reflecting neurite density (NDI); orientation dispersion (ODI), quantifying neurite orientation variability; and isotropic volume fraction (F_{ISO}), representing free water content. NODDI maps were normalized to the high-resolution FMRIB58_FA standard space image using the inverse DTI transformation matrix, ensuring alignment with other diffusion-derived metrics. Average NDI, ODI, and F_{ISO} values were then extracted across the four DTI-ALPS ROIs.

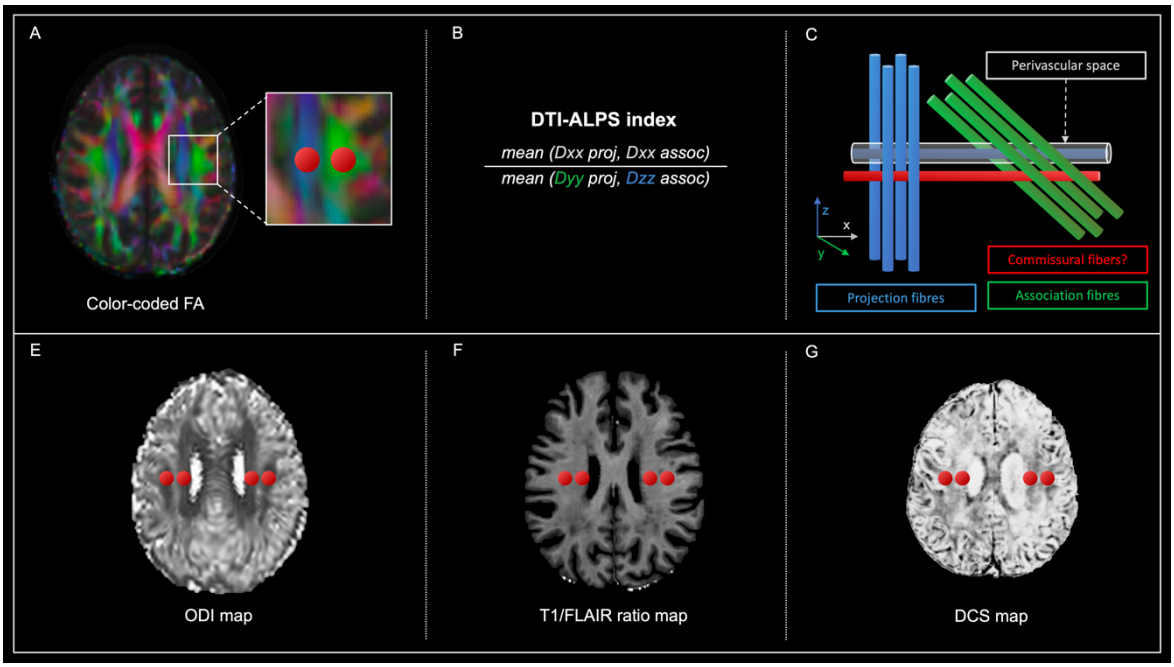

Figure 2. Illustration of the DTI-ALPS index and related microstructural MRI metrics. (A) Color-coded fractional anisotropy (FA) map showing regions of interest (red circles) in projection and association fiber areas within the centrum semiovale of both hemispheres. (B) Formula of the DTI-ALPS index, expressing diffusivity along perivascular spaces plane relative to orthogonal fiber orientations. (C) Schematic representation of projection (*blue*), association (*green*), and commissural (*red*) fibers, and their relationship to the perivascular space (*grey*). (E–G) Corresponding quantitative MRI maps with superimposed DTI-ALPS ROIs: (E) Orientation Dispersion Index (ODI) from NODDI, indicating fiber complexity and dispersion (darker areas = less dispersion); (F) T1/FLAIR ratio as a proxy for myelin content (brighter areas = more myelin); (G) Diamagnetic Component of Susceptibility (DCS) derived from QSM, reflecting diamagnetic contributions linked to myelin integrity (darker areas = more myelin).

3.6 Statistical analysis

All statistical analyses were performed using R Studio (version 2025.09.1+401, R Foundation for Statistical Computing, Vienna, Austria). Data were first examined using descriptive statistics and visual inspection of distributions to assess normality.

Exploratory analyses were conducted to evaluate associations between the main study variables and demographic factors. Associations with age were tested using linear models (including both linear and quadratic terms to capture potential nonlinear effects), and associations with sex were assessed using two-sample t-tests. Pairwise correlations among continuous variables were computed using Pearson's correlation coefficients, with two-tailed p-values adjusted for multiple comparisons using the False Discovery Rate (FDR) correction. Statistical significance was set at $p < 0.05$ (FDR-corrected).

Variables that showed significant correlations with DTI-$ALPS_{1000}$ after FDR correction were further analyzed using multivariate linear regression models after scaling, with the DTI-$ALPS_{1000}$ as the primary dependent variable, adjusting for age (linear and quadratic terms) and sex. Model performance was assessed by computing the adjusted coefficient of determination ($adjR^2$), Akaike information criterion (AIC), and Bayesian information criterion (BIC).

An exploratory factor analysis (EFA) was then performed on the residuals of variables that remained significant after the regression analyses, thus using data adjusted for the effects of age and sex. We note that this represents a more aggressive correction, owing to potential shared variance between WM metrics and age. The suitability of the dataset for factor analysis was verified using the Kaiser–Meyer–Olkin (KMO) measure of sampling adequacy (threshold > 0.6, both overall and for each variable) and by confirming the absence of multicollinearity (pairwise r <0.8). The EFA was conducted with the psych package in R[76]. The optimal number of factors to retain was determined using the fa.parallel function based on parallel analysis. Factor extraction was performed with the minimum residual (minres) method, and factors were rotated using oblimin rotation to allow for correlated components. Model fit was assessed using Root Mean Square Error of Approximation (RMSEA), Tucker–Lewis Index (TLI) and Root Mean Square Residual (RMSR).

4. RESULTS

4.1 Demographic and clinical characteristics of the study population

Of the 100 subjects included in the study, 20 were CU elderly subjects, 21 sMCI patients, 39 AD patients, 20 patients with non-AD neurodegenerative conditions. The demographics for the whole cohort and each group separately are detailed in **Table 2**.

Table 2. **Clinical and demographical data of the patients**

	All n=100	CU n=20	sMCI n=21	AD n=39	Non-AD n=20	Statistic[a]	
Age, years (Q1,Q3)	73 (66,76)	69 (60,75)	74 (69,76)	62 (66.5, 76.5)	75.5 (70.75,78)	*χ2*	6.43
						p	0.09
Sex, Females:Males	54:46	7:13	12:9	22:17	13:7	*χ2*	4.01
						p	0.26
Years of Education (Q1,Q3)	13 (8,18)	13 (8,18)	8 (8,13)	13 (12,18)	13 (7.75,14.25)	*χ2*	6.82
						p	0.08
MMSE at MRI (Q1,Q3)	26* (23,28)	29 (28.75,30)	26 (25,28)	23 (21, 26)	24.3 (22,26)	*χ2*	40.72
						p	**<0.001**
FDG-PET, Y:N	46:54	8:12	9:12	15:24	14:6	-	-
FBB-PET, Y:N	27:73	7:13	5:16	11:28	4:16	-	-
CSF, Y:N	48:52	5:15	8:13	24:15	11:9	-	-

Abbreviations: *CU*: cognitively unimpaired; *sMCI*: stable mild cognitive impairment; *AD*: Alzheimer's disease; *Non-AD*: Non-Alzheimer's disease dementias; *MMSE*: mini-mental state examination; *FDG-PET*: fluorodeoxyglucose positron emission tomography; *FBB-PET*: fluorbetaben positron emission tomography; *CSF*: cerebrospinal fluid. *a:* Reported P-values from one-way between-groups ANOVA for age, years of education, MMSE at MRI, and chi-square test fo indipende for sex, FDG-PET, FBB-PET and CSF.

There was no significant difference in sex distribution, age and years of education across the groups. A significant difference in MMSE at the time of MRI was observed ($p<0.001$), with pairwise comparisons revealing that the CU group had significant higher scores than all the other groups ($p<0.001$ for all comparisons) and that sMCI patients had higher values compared to AD patients ($p<0.014$).

All DTI measures at both b-values showed a linear effect of age (**see Supplementary figure 1 and 2** for R^2 for linear and quadratic components), except for FA. ODI and NDI, but not F_{ISO}, showed a linear reduction with age.

Among structural metrics, $T1/FLAIR_{ratio}$ tended to decrease and DCS_{kurt} to increase quadratically with age, while DCS_{std} show a linear increase and DCS_{skew} a linear decrease with age. All other DCS metrics showed no relation with age.

Many measures exhibited a main effect of sex. Particularly, FA_{1000}, FA_{2000}, MA_{1000}, were higher in men, while DCS_{mean}, DCS_{med}, DCS_{p10}, DCS_{p25}, DCS_{p75}, DCS_{p90} and $T1/FLAIR_{ratio}$ were higher in females. There were no sex differences in NODDI related metrics.

4.2 DTI-ALPS$_{1000}$ is inversely associated with FA and MD in the DTI-ALPS ROIs

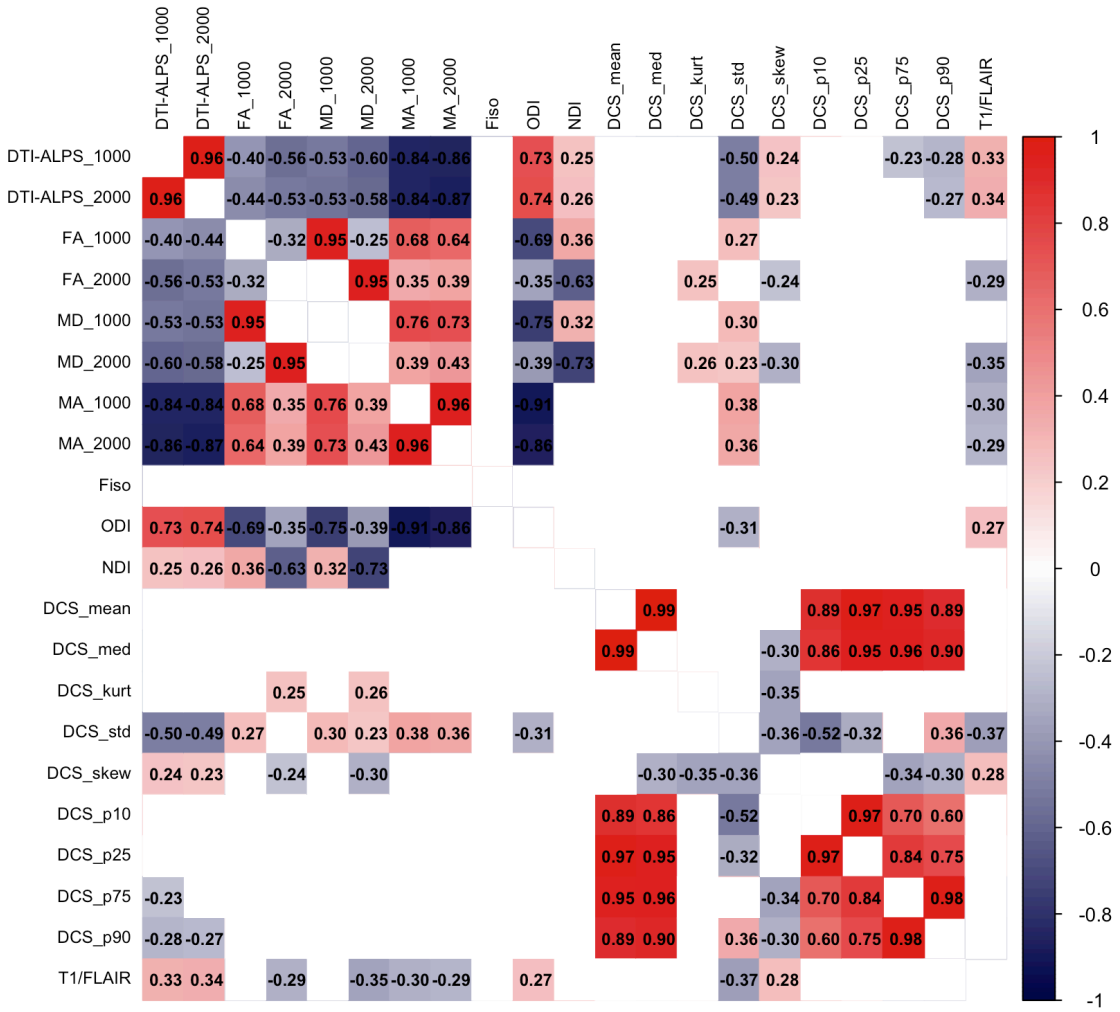

Figure 3. **Correlation matrix of variables of interest**. Positive correlations are shown in red and negative correlations in blue. Only statistically significant associations after FDR correction are displayed. Pearson's r values are reported within the squares.

Figure 3 shows the correlations between the main study variables, and **Figure 4** displays the strongest associations through size- and symbol-coded scatterplots**.** A reduction in the DTI-ALPS$_{1000}$ values was associated with an increase in FA_{1000} and MD_{1000} (r=-0.40; r=-0.56 respectively, all p_{FDR}<0.001). Stronger correlations were found with FA_{2000} and MD_{2000}

(r=-0.53; r=-0.60 respectively, all p_{FDR}<0.001). After correction for age and sex in multivariate models, FA and MD at both b-values remained significant predictors of DTI-ALPS$_{1000}$. (**Supplementary table 1**). AIC and BIC were consistently lower and adjR^2 higher when considering measures extracted at b=2000.

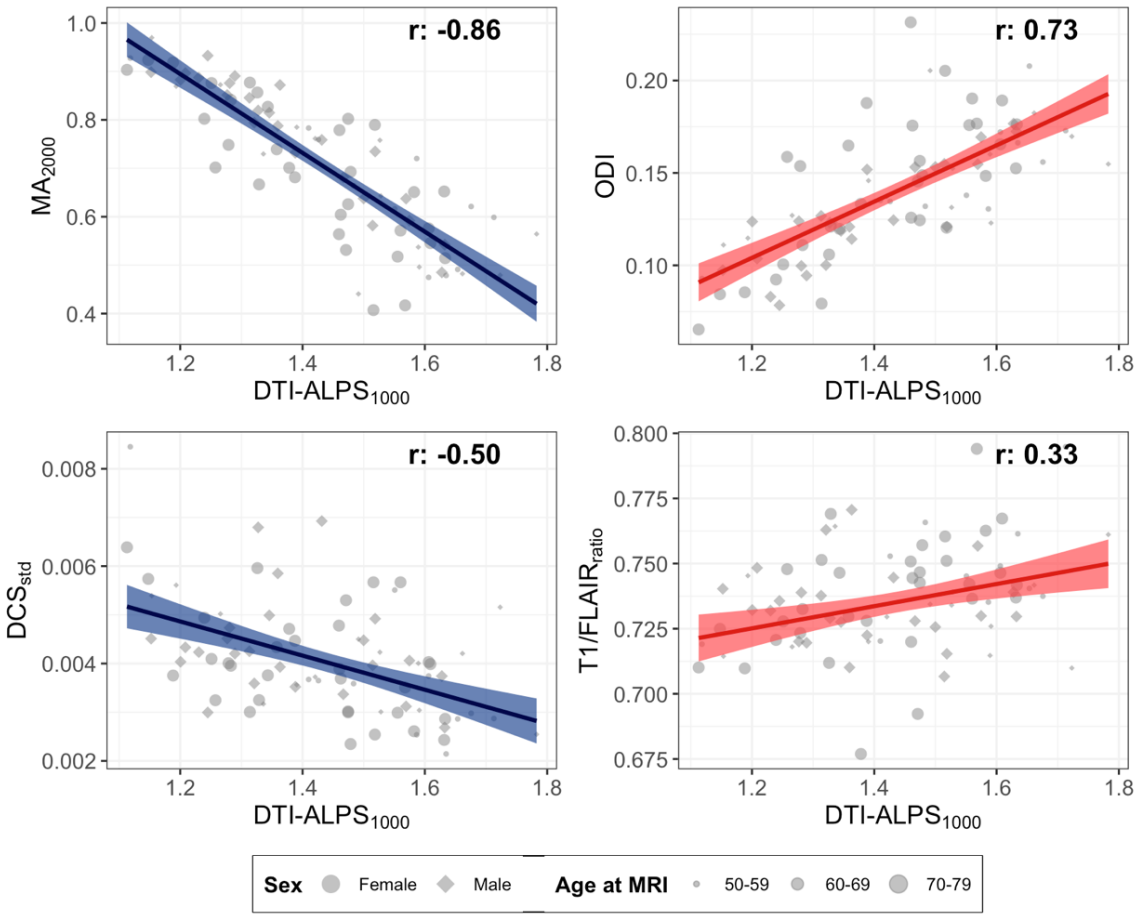

Figure 4. Bubble plots illustrating relationships between DTI-ALPS$_{1000}$ and selected variables. Size scales with age, and marker shape denotes sex. Negative and positive correlations with DTI-ALPS$_{1000}$ are shown by blue and red regression lines, respectively, with shaded areas representing standard error.

4.3 DTI-ALPS$_{1000}$ is strongly and inversely associated with MA in DTI-ALPS ROIs

A reduction in DTI-ALPS$_{1000}$ values was strongly associated with an increase in MA$_{1000}$ and even higher increases in MA$_{2000}$ (r = –0.84 and r = –0.86, respectively; all p_{FDR}<0.001). Both MA$_{1000}$ and MA$_{2000}$ remained robust independent predictors of ALPS after adjustment for age and sex (**Supplementary table 1**). Model fit indices were consistently lower, and explained variance higher, when measures derived from the b=2000 shell were used.

4.4 DTI-ALPS$_{1000}$ is highly and directly associated with ODI in the ALPS ROIs

DTI-ALPS$_{1000}$ showed a strong positive correlation with ODI (r 0.73, p_{FDR}<0.001). We also found a weaker positive association with NDI (r 0.25, p_{FDR}=0.030). ODI showed also a strong negative correlation with MA at both b=1000 and b=2000 (r -0.91 and -0.86 respectively, all p_{FDR}<0.001).

In the multivariate model, only ODI remained a significant independent predictor of DTI-ALPS$_{1000}$ (**Supplementary table 1**).

4.5 DTI-ALPS$_{1000}$ values show moderate associations with structural WM markers

When considering structural MRI metrics, DTI-ALPS$_{1000}$ values showed a direct association with T1/FLAIR$_{ratio}$ (r=0.33, p_{FDR}=0.003) and with DCS$_{skew}$ (r=0.24, p_{FDR}=0.037). On the other hand, DTI-ALPS$_{1000}$ showed a strong negative correlation with DCS$_{std}$ (r=-0.50, p_{FDR}<0.001) and moderate association with DCS$_{p75}$ and DCS$_{p90}$ (r=-0.23, p_{FDR}=0.045; r=-0.28, p_{FDR}=0.012 respectively).

T1/FLAIR$_{ratio}$ was negatively associated with MA$_{1000}$ (r -0.30, p_{FDR}=0.006 FDR), MA$_{2000}$ (r -0.29, p_{FDR}=0.010), MD$_{1000}$ (r -0.29, p_{FDR}=0.008) and MD$_{2000}$ (r -0.35, p_{FDR}=0.001), while positively correlated with ODI (r 0.27, p_{FDR}=0.018). DCS$_{std}$ showed the opposite pattern: it was positively associated with MA$_{1000}$ (r 0.38, p_{FDR}<0.001), MA$_{2000}$ (r 0.36, p_{FDR}<0.001), FA$_{1000}$ (r 0.27, p_{FDR} =0.016), FA$_{2000}$ (r 0.30, p_{FDR}=0.008) and MD$_{2000}$ (r 0.23, p_{FDR}=0.046), while negatively correlated with ODI (r -0.31, p_{FDR}=0.006)

DCS$_{std}$, DCS$_{p75}$, DCS$_{p90}$ and T1/FLAIR$_{ratio}$ remained significant predictors of DTI-ALPS$_{1000}$ after correcting for age and sex. By contrast DCS$_{skew}$ became unsignificant (**Supplementary table 1**).

4.6 DTI-ALPS$_{1000}$ associates with diffusion anisotropy metrics in factor analysis

Prior to factor extraction, three variables were excluded: FA and MD at both b-values, which showed low sampling adequacy (KMO < 0.6) and DCS$_{p75}$, which exhibited high collinearity with DCS$_{p90}$. ODI, MA$_{1000}$ and MA$_{2000}$ showed high collinearity, leading to Heywood case when kept together in the model. However, as these were the primary variables of interest, rather than excluding one, we conducted two separate EFAs—one retaining ODI and the other retaining MA$_{2000}$ (MA$_{1000}$ was excluded due to high collinearity and its weaker correlation with DTI-ALPS$_{1000}$).

Considering ODI, a two-factor solution provided the best fit to the data (χ^2 = 0.42, p = 0.52; RMSEA = 0.00, 90% CI = [0, 0.23]; TLI = 1.06; RMSR = 0.01), accounting for 54% of the total variance (Factor 1 = 29%; Factor 2 = 25%). Factor 1 loaded primarily on DTI-ALPS$_{1000}$ (β=0.62) and ODI (β=1.01), whereas Factor 2 was driven by DCS$_{std}$ (β=0.90) and DCS$_{p90}$

(β=0.42), with smaller contributions from $T1/FLAIR_{ratio}$ (β=–0.33). The two factors were moderately correlated (r –0.32), indicating partially overlapping latent constructs. The model demonstrated excellent fit and high factor score reliability (minimum correlation = 0.66–0.97).

When MA_{2000} was retained, results were almost alike. A two-factor solution provided an adequate fit to the data (χ^2 = 2.6, p = 0.11; RMSEA = 0.13, 90% CI = [0, 0.33]; TLI = 0.90; RMSR = 0.02), explaining 56% of the total variance (Factor 1 = 33%; Factor 2 = 23%). Factor 1 loaded primarily on MA_{2000} (β=1.03) and inversely on $DTI\text{-}ALPS_{1000}$ (β=–0.75), while Factor 2 was driven by DCS_{std} (β=0.83) and, to a lesser extent, by DCS_{p90} (β=0.48) and $T1/FLAIR_{ratio}$ (β=–0.35). The two factors were moderately correlated (r 0.39), suggesting partially overlapping latent dimensions. Model fit indices indicated good adequacy, with a TLI of 0.895 and strong factor score reliability (minimum correlation = 0.53–0.99)(**Figure 5**).

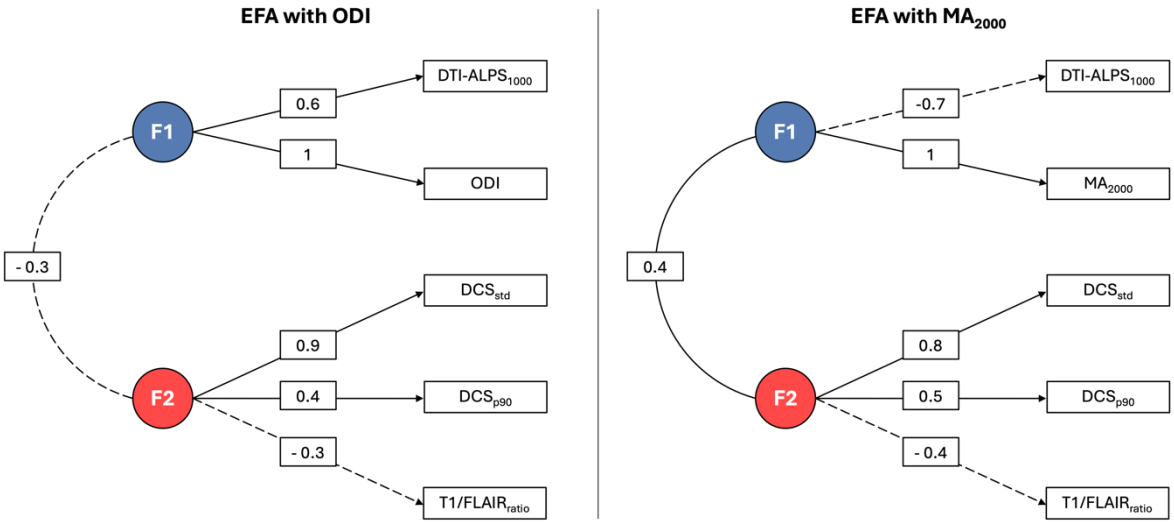

Figure 5. Exploratory factor analysis models including either ODI or MA_{2000}. The two models show latent factors (F_1, F_2) and their standardized loadings onto diffusion and structural metrics. Dashed arrows indicate negative loadings, and numbers represent standardized factor loadings or inter-factor correlations. Model including ODI (*left*); model including MA_{2000} *(right)*.

5. DISCUSSION

In this study, we aimed to characterize the determinants of DTI-ALPS changes in neurodegenerative diseases using a clinical MRI protocol incorporating multi-shell DWI and structural MRI. We found that DTI-ALPS, calculated at b=1000, is highly associated with DTI measure of diffusion anisotropy, particularly MA and ODI, and demonstrates a moderate relationship with structural markers of WM microstructural damage, namely $T1/FLAIR_{ratio}$ and DCS.

Overall, our findings suggest that DTI-ALPS predominantly reflects loss of crossing fibers and WM microstructural damage within the ROIs where it is calculated, rather than serving as a direct measure of glymphatic function, as originally proposed. We substantiate this interpretation in greater detail in the following paragraphs.

In the original paper by Taoka, DTI-ALPS was proposed as a marker of glymphatic activity based on the hypothesis that in an area “in which conformation of the perivascular space, represented by medullary veins on SWI, and the major white matter tracts were perpendicular to each other”, the “ratio of x-axis diffusivity in the projection fibers (i.e. corticospinal tract) and association fibers (i.e. superior longitudinal fasciculus) area (Dxproj and Dxassoc) to the diffusivity which is perpendicular to them (Dyproj and Dzassoc) would express the influence of the water diffusion along the perivascular space which will reflect activity of the glymphatic system in the individual cases”[21].

Therefore, for DTI-ALPS to truly represent glymphatic activity, changes in the index should primarily arise from variations in x-axis diffusivity (Dxx), which is hypothesized to be most sensitive to perivascular fluid movement.

Considering the main orientation of eigenvector-2 in these tracts, the DTI-ALPS index can be approximated as ≈ λ2/λ3, assuming similar λ2/λ3 ratios for the two fibers types[35].

Consequently, and all else being equal, a reduction in glymphatic flow would be expected to increase FA anisotropy within DTI-ALPS-ROIs and decrease MD, due to the reduction of λ2 component. In addition, it would result in a reduction of radial asymmetry (i.e the ratio between λ2 and λ3)[33,35].

Even if reduced glymphatic flow were instead to result in fluid stagnation and an increase in free water content, the ensuing diffusion pattern would be expected to become more isotropic and once again characterized by decreased FA and increased MD. This latter pattern is typical of WM damage and axonal degeneration, where expansion of the extracellular space occurs secondary to axonal loss[40].

In our cohort, however, we observed an inverse correlation between DTI-ALPS index and both FA and MD within the DTI-ALPS ROIs, a finding that may initially seem counterintuitive. Nonetheless, a small number of prior studies have reported parallel

increases in FA[44,77–79] and MD[78] in AD, Parkinson's disease and progressive supranuclear palsy[34], particularly in the centrum semiovale[78].

These parallel increases of FA and MD have been attributed to the selective degeneration of crossing fibers—a hypothesis supported by multiple converging lines of evidence: (i) the centrum semiovale, from which DTI-ALPS is derived, is densely packed with crossing bundles[36,37]; (ii) AD is characterized by early degeneration of intracortical association fibers, with relative preservation of corticofugal and corticopetal tracts[80] (iii) Increases in FA and MD were accompanied by a corresponding rise in MA[44,77]; (iv) quantitative tractography indicated that this effect was directly related to the selective sparing of motor-related projection fibers[77,78].

Indeed, the colocalized increase in MA within such crossing-fiber regions suggests a transition of the WM bundles toward a more linear ("cigar-like") shape, consistent with loss of crossing fibers.

In line with this evidence, we found that MA alone explained more than 75% of the variance in DTI-ALPS, strongly suggesting that DTI-ALPS primarily reflects the integrity of crossing fibers rather than perivascular diffusion.

Given the assumptions outlined above and the sensitivity of DTI to extracellular free water, a reduction in λ_2 diffusivity—presumed to reflect perivascular glymphatic flow (Dxx)—could theoretically increase FA and thus MA. However, several lines of evidence argue against a substantial glymphatic contribution to the parallel changes observed in MA and DTI-ALPS.

First, if DTI-ALPS were sensitive to perivascular diffusion, its correlations with DTI metrics would be strongest at lower b-values (i.e. b=1000 s/mm²). Instead, we found stronger associations at higher b-values (i.e. b=2000 s/mm²), reinforcing the view that DTI-ALPS is primarily driven by axonal microstructure, as already reported[33–35].

Second, perivascular spaces occupy only about 1% of the WM volume[31,81], representing a negligible fraction of the DTI-ALPS ROIs too. Even assuming some sensitivity of DTI-ALPS to glymphatic dynamics, the association with MA_{2000} should display considerable interindividual variability, given (i) expected differences in the relative contributions of glymphatic and microstructural effects across subjects, and (ii) opposing influences of glymphatic flow reduction on FA—potentially increasing FA through decreased λ_2 while simultaneously decreasing FA through extracellular fluid accumulation[25,26]. This would produce greater scatter in the DTI-ALPS–MA relationship than we observed.

Third, we found moderate correlations between DTI-ALPS and structural MRI indices of WM integrity, particularly $T1/FLAIR_{ratio}$ and DCS_{std}. Although the association between DTI-ALPS and conventional DTI metrics was weaker—likely reflecting the greater sensitivity of diffusion imaging to subtle microstructural changes[78]—these findings support a link between DTI-ALPS and WM damage. Specifically, the positive correlation between DTI-

ALPS and the T1/FLAIR$_{ratio}$ suggests that lower DTI-ALPS values correspond to reduced tissue integrity. The T1/FLAIR$_{ratio}$ has been proposed as a practical alternative to the T1/T2 ratio for assessing myelin-related properties[51], given the widespread use of volumetric FLAIR over T2-weighted sequences in current MRI protocols. Despite concerns about its specificity for myelin, based on comparisons with other myelin mapping modalities[82–84] and post-mortem studies[85–87], the T1/FLAIR$_{ratio}$ remains a valuable composite marker of tissue integrity reflecting contributions from myelin, iron, calcium, axonal density, and extracellular content[51,83]. It has also been proposed as a sensitive, clinically accessible marker of WM damage in neurodegenerative disorders[52,53]. Accordingly, its reduction in DTI-ALPS ROIs supports the interpretation that WM damage confounds DTI-ALPS metrics.
A similar interpretation applies to DCS. We hypothesized that lower DTI-ALPS values would correspond to higher DCS—reflecting myelin loss, as previously reported in AD[56]. Although a trend toward increased mean and median DCS within DTI-ALPS ROIs was observed, it did not reach statistical significance. However, DTI-ALPS showed a strong inverse correlation with DCS$_{std}$ and a moderate inverse correlation with DCS$_{p90}$. Together, these findings suggest that (i) a reduction of DTI-ALPS is associated with a shift toward higher DCS values, consistent with demyelination[56,88], and (ii) lower DTI-ALPS coincides with greater DCS variability, indicative of increased microstructural heterogeneity, in agreement with T1/FLAIR$_{ratio}$ results. While susceptibility measures can be affected by fiber orientation relative to the main magnetic field, averaging across two orthogonal ROI sets likely minimized this confound[89].
Fourth, DTI-ALPS showed a strong positive correlation with ODI, which was itself closely related to MA. Reduced ODI has been consistently reported in neurodegenerative diseases and interpreted as a consequence of selective loss of crossing fibers[47,90,91], leading to greater alignment of remaining axons. ODI has also demonstrated stronger histological validity than DTI metrics[92,93], likely because it corrects for the biasing effect of extracellular free water. Moreover, as ODI derives from the neurite compartment within the NODDI framework, its relationship with DTI-ALPS reinforces the view that ALPS primarily captures axonal geometry rather than perivascular flow.
Although MA, ODI, and structural indices of WM damage accounted for most of the DTI-ALPS variance, a small portion remained unexplained. This residual variance, however, should not automatically be attributed to glymphatic activity, as it may instead reflect unmodelled biological or methodological factors.
Indeed, EFA clearly revealed that DTI-ALPS do not form a distinct component but instead clusters with MA and ODI, indicating that it largely reflects neurite orientation and diffusion coherence rather than a separate physiological process.

Moreover, it is important to note that the DTI-ALPS index primarily reflects the radial asymmetry of underlying tracts[33,35], which depends not only on crossing fibers but also on microscopic features of the fascicles—such as dispersion anisotropy and axonal undulation. These microscopic features may be less effectively detected by MA and ODI, requiring more advanced modeling taking into account also non isotropic dispersion[94].
Finally, the small fraction of variance left unexplained by MA, ODI and structural MRI markers may simply reflect measurement noise. In this context, the imperfect alignment between WM tracts and reference axes merits specific consideration. Because diffusion tensor eigenvectors rarely coincide exactly with these axes, even minor misalignments can introduce discrepancies between MA and DTI-ALPS despite their shared microstructural basis. To verify this assumption, we calculated a modified version of MA substituting eigenvalues with corresponding diffusion axes in the ROIs, which led to an increase in the proportion of DTI-ALPS variance explained—particularly at b=2000—further supporting their common structural origin (**Supplementary table 2**).

6. LIMITATIONS

This study has several limitations. First, diffusion data were acquired with a maximum b-value of 2000 s/mm², which may not fully suppress the contribution of freely diffusing water. Higher b-values could enhance the sensitivity of diffusion metrics to tissue microstructure; however, the acquisition protocol was constrained by clinical MRI parameters to ensure feasibility in a patient population.

Second, the NODDI model used here assumes isotropic orientation dispersion, and thus does not account for potential anisotropic components that may better capture the complexity of white matter fiber geometry. Incorporating more advanced diffusion models (i.e Bingham NODDI)[94] could provide a more accurate description of microstructural dispersion patterns. Moreover, it could test if DTI-ALPS is able to capture reduction of dispersion linked to anisotropic components, as has been proposed.

Finally, the cross-sectional design limits the ability to determine how WM microstructural confounders influence the predictive validity of the DTI-ALPS index over time. Longitudinal studies are needed to determine whether the DTI-ALPS index maintains its predictive value in this context.

7. CONCLUSIONS

In conclusion, our study demonstrates that DTI-ALPS measures are strongly associated with WM microstructural integrity, as assessed through both DTI and structural MRI. Specifically, our findings suggest that DTI-ALPS metrics primarily reflect loss of crossing fibers and increased microstructural heterogeneity within DTI-ALPS ROIs, challenging its interpretation as a direct marker of glymphatic activity as originally proposed by Taoka. Nevertheless, our intention is not to fully dismiss ALPS—which remains the only putative glymphatic marker tested against intrathecal gadolinium[95]—but rather to emphasize the need for further validation and consensus. The sensitivity of the DTI-ALPS index to WM geometry (i.e., diffusion asymmetry) may still prove valuable for investigating WM damage in neurodegenerative diseases. Moreover, given the dependence of glymphatic clearance on normal microstructural anatomy, DTI-ALPS could still be proved a useful marker of glymphatic dysfunction secondary to WM injury, provided its correlation with gadolinium clearance in intrathecal CE-MRI is confirmed. However, current evidence—including our own—suggests that DTI-ALPS is influenced by WM microstructure and may not reliably represent a direct marker of glymphatic flow.

8. SUPPLEMENTARY MATERIALS

Supplementary table 1. Multivariate analysis results with DTI-ALPS$_{1000}$ as dependent variable

FA_1000

term	estimate	std.error	statistic	p.value sig
(Intercept)	-0.761	5.751	-0.132	0.895
FA_1000	-0.348	0.084	-4.134	**<0.001*** **
Age at MRI	0.089	0.172	0.518	0.606
Age at MRI^2	-0.001	0.001	-0.855	0.394
Sex	-0.102	0.168	-0.607	0.545
		adjR2: 0.341	**AIC**: 248.974	**BIC**: 264.605

FA_2000

term	estimate	std.error	statistic	p.value sig
(Intercept)	-0.409	5.360	-0.076	0.939
FA_2000	-0.463	0.079	-5.834	**<0.001*** **
Age at MRI	0.073	0.160	0.453	0.652
Age at MRI^2	-0.001	0.001	-0.787	0.433
Sex	-0.039	0.158	-0.245	0.807
		adjR2: 0.427	**AIC**: 234.898	**BIC**: 250.529

MD_1000

term	estimate	std.error	statistic	p.value sig
(Intercept)	-0.712	5.479	-0.130	0.897
MD_1000	-0.451	0.085	-5.337	**<0.001*** **
Age at MRI	0.070	0.164	0.425	0.672
Age at MRI^2	-0.001	0.001	-0.665	0.508
Sex	-0.321	0.157	-2.050	**0.043***
		adjR2: 0.402	**AIC**: 239.289	**BIC**: 254.92

MD_2000

term	estimate	std.error	statistic	p.value sig
(Intercept)	0.577	5.409	0.107	0.915
MD_2000	-0.487	0.086	-5.654	**<0.001*** **
Age at MRI	0.025	0.162	0.155	0.877
Age at MRI^2	0.000	0.001	-0.363	0.717
Sex	-0.326	0.154	-2.110	**0.037***
		adjR2: 0.418	**AIC**: 236.51	**BIC**: 252.141

MA_1000

term	estimate	std.error	statistic	p.value sig
(Intercept)	-0.591	3.619	-0.163	0.871
MA_1000	-0.779	0.057	-13.711	**<0.001*** **
Age at MRI	0.045	0.108	0.419	0.676
Age at MRI^2	-0.001	0.001	-0.655	0.514
Sex	0.075	0.106	0.707	0.481
		adjR2: 0.739	**AIC:** 156.36	**BIC:** 171.991

MA_2000

term	estimate	std.error	statistic	p.value sig
(Intercept)	0.301	3.536	0.085	0.932
MA_2000	-0.787	0.055	-14.196	**<0.001*** **
Age at MRI	0.017	0.106	0.156	0.876
Age at MRI^2	0.000	0.001	-0.372	0.711
Sex	-0.001	0.102	-0.013	0.990
		adjR2: 0.751	**AIC**: 151.684	**BIC:** 167.315

ODI

term	estimate	std.error	statistic	p.value sig

NDI

term	estimate	std.error	statistic	p.value sig

(Intercept)	-1.670	4.495	-0.371	0.711
ODI	0.641	0.068	9.409	**<0.001*** **
Age at MRI	0.091	0.134	0.681	0.497
Age at MRI^2	-0.001	0.001	-0.951	0.344
Sex	-0.065	0.130	-0.502	0.617
		adjR2:	**AIC:**	**BIC:**
		0.597	199.67	215.301

(Intercept)	-0.682	6.227	-0.109	0.913
NDI	0.083	0.095	0.873	0.385
Age at MRI	0.089	0.186	0.477	0.635
Age at MRI^2	-0.001	0.001	-0.787	0.433
Sex	-0.267	0.177	-1.505	0.136
		adjR2:	**AIC:**	**BIC**:
		0.229	264.715	280.346

DCS_std

term	**estimate**	**std.error**	**statistic**	**p.value sig**
(Intercept)	-2.883	5.641	-0.511	0.610
DCS_std	-0.393	0.084	-4.705	**<0.001*** **
Age at MRI	0.143	0.168	0.851	0.397
Age at MRI^2	-0.001	0.001	-1.143	0.256
Sex	-0.158	0.162	-0.978	0.331
	adjR2:	**AIC:**	**BIC:**	
	0.369	244.566	260.197	

DCS_skew

term	**estimate**	**std.error**	**statistic**	**p.value sig**
(Intercept)	-0.295	6.229	-0.047	0.962
DCS_skew	0.104	0.092	1.129	0.262
Age at MRI	0.077	0.186	0.415	0.679
Age at MRI^2	-0.001	0.001	-0.726	0.470
Sex	-0.248	0.177	-1.396	0.166
	adjR2:	**AIC:**	**BIC:**	
	0.233	264.181	279.812	

DCS_p75

term	**estimate**	**std.error**	**statistic**	**p.value sig**
(Intercept)	0.002	6.090	0.000	1.000
DCS_p75	-0.211	0.091	-2.318	**0.023***
Age at MRI	0.069	0.182	0.381	0.704
Age at MRI^2	-0.001	0.001	-0.696	0.488
Sex	-0.375	0.180	-2.087	**0.040***
	adjR2:	**AIC:**	**BIC:**	
	0.264	260.012	275.643	

DCS_p90

term	**estimate**	**std.error**	**statistic**	**p.value sig**
(Intercept)	-0.058	6.012	-0.010	0.992
DCS_p90	-0.252	0.090	-2.798	**0.006***
Age at MRI	0.070	0.180	0.387	0.699
Age at MRI^2	-0.001	0.001	-0.698	0.487
Sex	-0.391	0.177	-2.207	**0.030***
	adjR2:	**AIC:**	**BIC:**	
	0.282	257.597	273.228	

T1/FLAIR_ratio

term	**estimate**	**std.error**	**statistic**	**p.value sig**
(Intercept)	1.858	6.264	0.297	0.767
T1/FLAIR_ratio	0.194	0.095	2.041	**0.044***
Age at MRI	0.009	0.188	0.047	0.962
Age at MRI^2	0.000	0.001	-0.342	0.733
Sex	-0.173	0.180	-0.961	0.339

Abbreviations: *FA*: fractional anisotropy (b=1000, b=2000); *MD*: mean diffusivity (b=1000, b=2000); *MA*: mode of anisotropy (b=1000, b=2000); ODI: orientation dispersion index; *NDI*: neurite density index; DCS: diamagnetic component of susceptibilty (standard deviation,skewness,10th percentile, 90th percentile). All results are based on scaled variables and reported as standardized estimates. Significant results are in bold. *p<0.05; **p<0.005; ***p<0.001

Supplementary table 2. Multivariate analysis for modified mode of anisotropy using DTI-ALPS$_{1000}$ as dependent variable

mMA_1000

term	estimate	std.error	statistic	p.value sig
(Intercept)	0.750	3.480	0.215	0.830
mMA_1000	-3.265	0.225	-14..539	**<0.001*****
Age at MRI	0.061	0.104	0.589	0.557
Age at MRI^2	-0.001	0.001	-0.811	0.420
Sex	0.131	0.103	1.277	0.205
		adjR2: 0.759	**AIC**: 148.42	**BIC**: 164.05

mMA_2000

term	estimate	std.error	statistic	p.value sig
(Intercept)	3.461	3.303	1.048	0.297
mMA_2000	-4.220	0.268	-15.721	**<0.001*****
Age at MRI	0.001	0.098	0.003	0.998
Age at MRI^2	-0.001	0.001	-0.157	0.875
Sex	0.019	0.096	0.201	0.841
		adjR2: 0.784	**AIC**: 137.38	**BIC**: 153.01

Abbreviations: *mMA*: modified mode of anisotropy. All results are based on scaled variables and reported as standardized estimates. Significant results are in bold. *p<0.05; **p<0.005; ***p<0.001

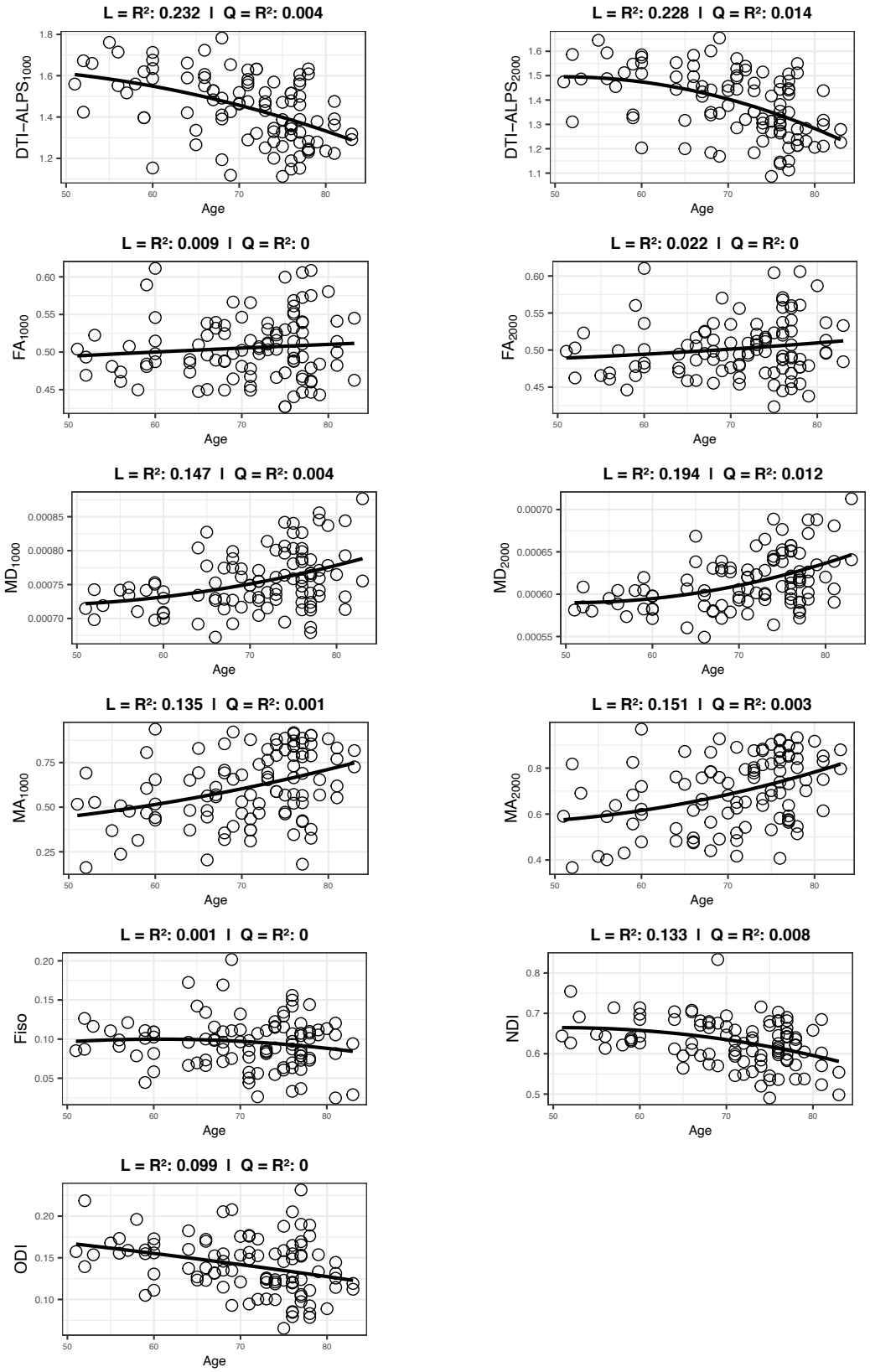

Supplementary figure 1. **Scatterplot grid showing associations between diffusion-derived metrics and age.** Each panel depicts the relationship between a diffusion metric and age, modeled with both linear and quadratic components. Solid lines represent fitted polynomial regression curves.

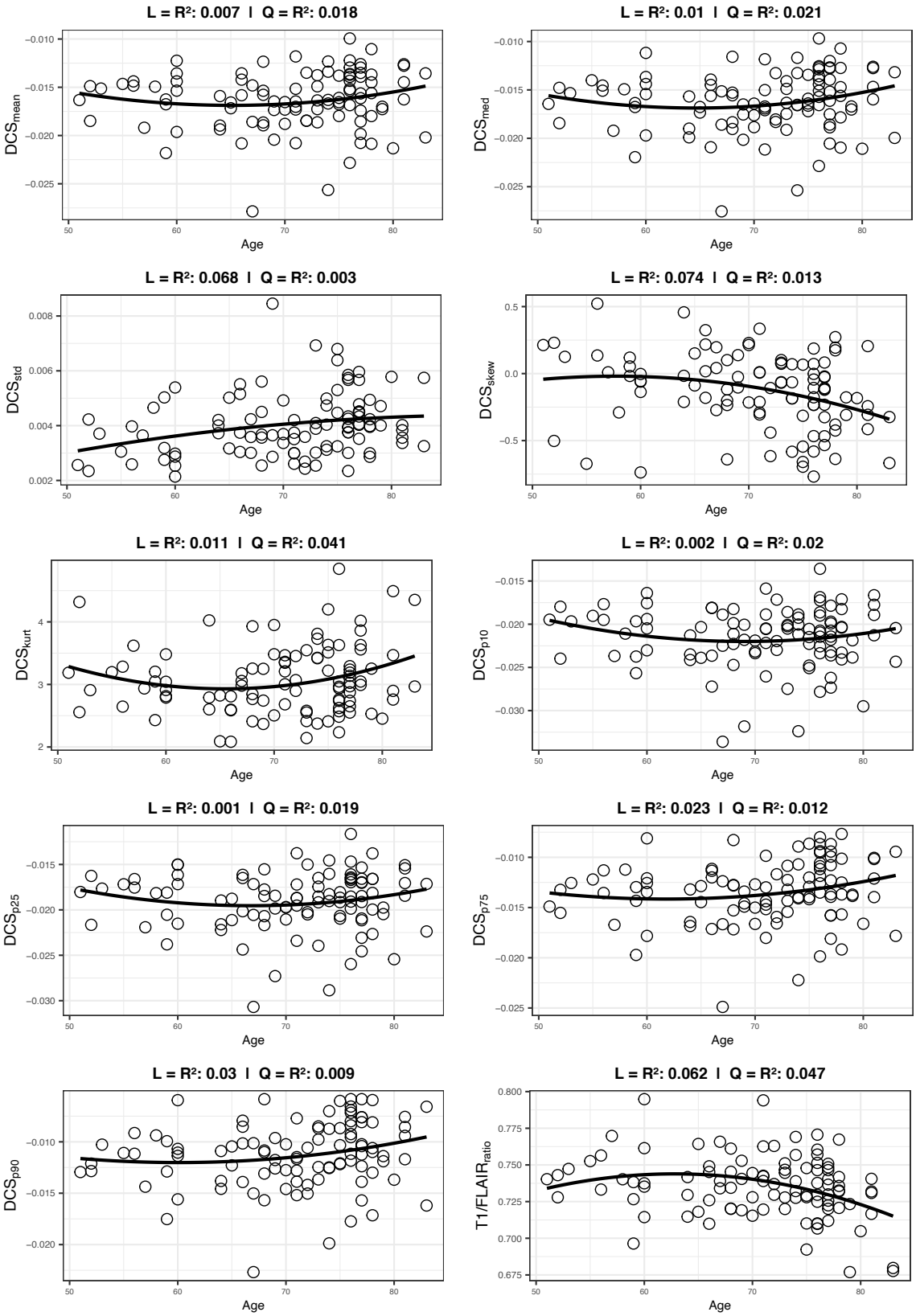

Supplementary figure 2. Scatterplot grid showing associations between structural MRI-derived metrics and age. Each panel depicts the relationship between a structural MRI metric and age, modeled with both linear and quadratic components. Solid lines represent fitted polynomial regression curves.

9. REFERENCES

1. Rasmussen MK, Mestre H, Nedergaard M. The glymphatic pathway in neurological disorders. The Lancet Neurology [Internet]. 2018 [cited 2022 Sep 1];17:1016–24. https://doi.org/10.1016/S1474-4422(18)30318-1

2. Nedergaard M, Goldman SA. Glymphatic failure as a final common pathway to dementia. Science [Internet]. 2020 [cited 2023 Oct 24];370:50–6. https://doi.org/10.1126/science.abb8739

3. Kipnis J. The anatomy of brainwashing. Science [Internet]. 2024 [cited 2025 Oct 5];385:368–70. https://doi.org/10.1126/science.adp1705

4. Iliff JJ, Wang M, Liao Y, Plogg BA, Peng W, Gundersen GA, et al. A Paravascular Pathway Facilitates CSF Flow Through the Brain Parenchyma and the Clearance of Interstitial Solutes, Including Amyloid β. Sci Transl Med [Internet]. 2012 [cited 2022 Sep 1];4. https://doi.org/10.1126/scitranslmed.3003748

5. Aspelund A, Antila S, Proulx ST, Karlsen TV, Karaman S, Detmar M, et al. A dural lymphatic vascular system that drains brain interstitial fluid and macromolecules. Journal of Experimental Medicine [Internet]. 2015 [cited 2023 Oct 26];212:991–9. https://doi.org/10.1084/jem.20142290

6. Louveau A, Smirnov I, Keyes TJ, Eccles JD, Rouhani SJ, Peske JD, et al. Structural and functional features of central nervous system lymphatic vessels. Nature [Internet]. 2015 [cited 2023 Oct 26];523:337–41. https://doi.org/10.1038/nature14432

7. Smyth LCD, Xu D, Okar SV, Dykstra T, Rustenhoven J, Papadopoulos Z, et al. Identification of direct connections between the dura and the brain. Nature [Internet]. 2024 [cited 2025 Oct 6];627:165–73. https://doi.org/10.1038/s41586-023-06993-7

8. Kolabas ZI, Kuemmerle LB, Perneczky R, Förstera B, Ulukaya S, Ali M, et al. Distinct molecular profiles of skull bone marrow in health and neurological disorders. Cell [Internet]. 2023 [cited 2025 Oct 6];186:3706-3725.e29. https://doi.org/10.1016/j.cell.2023.07.009

9. Herisson F, Frodermann V, Courties G, Rohde D, Sun Y, Vandoorne K, et al. Direct vascular channels connect skull bone marrow and the brain surface enabling myeloid cell migration. Nat Neurosci [Internet]. 2018 [cited 2025 Oct 6];21:1209–17. https://doi.org/10.1038/s41593-018-0213-2

10. Bruner E, Eisová S. Vascular microforamina and endocranial surface: Normal variation and distribution in adult humans. The Anatomical Record [Internet]. 2024 [cited 2025 Oct 6];307:3375–83. https://doi.org/10.1002/ar.25426

11. Rasmussen MK, Mestre H, Nedergaard M. Fluid transport in the brain. Physiological Reviews [Internet]. 2022 [cited 2023 Oct 26];102:1025–151. https://doi.org/10.1152/physrev.00031.2020

12. Rustenhoven J, Kipnis J. Brain borders at the central stage of neuroimmunology. Nature [Internet]. 2022 [cited 2025 Oct 6];612:417–29. https://doi.org/10.1038/s41586-022-05474-7

13. Lopes DM, Wells JA, Ma D, Wallis L, Park D, Llewellyn SK, et al. Glymphatic inhibition exacerbates tau propagation in an Alzheimer's disease model. Alz Res Therapy [Internet]. 2024 [cited 2024 May 17];16:71. https://doi.org/10.1186/s13195-024-01439-2

14. Iliff JJ, Chen MJ, Plog BA, Zeppenfeld DM, Soltero M, Yang L, et al. Impairment of Glymphatic Pathway Function Promotes Tau Pathology after Traumatic Brain Injury. J Neurosci [Internet]. 2014 [cited 2023 Jan 14];34:16180–93. https://doi.org/10.1523/JNEUROSCI.3020-14.2014

15. Eide PK, Ringstad G. MRI with intrathecal MRI gadolinium contrast medium administration: a possible method to assess glymphatic function in human brain. Acta Radiologica Open [Internet]. 2015 [cited 2023 Oct 26];4:205846011560963. https://doi.org/10.1177/2058460115609635

16. Eide PK, Vinje V, Pripp AH, Mardal K-A, Ringstad G. Sleep deprivation impairs molecular clearance from the human brain. Brain [Internet]. 2021 [cited 2023 Oct 26];144:863–74. https://doi.org/10.1093/brain/awaa443

17. Eide PK, Ringstad G. Delayed clearance of cerebrospinal fluid tracer from entorhinal cortex in idiopathic normal pressure hydrocephalus: A glymphatic magnetic resonance imaging study. J Cereb Blood Flow Metab [Internet]. 2019 [cited 2023 Oct 26];39:1355–68. https://doi.org/10.1177/0271678X18760974

18. Lee S, Yoo R-E, Choi SH, Oh S-H, Ji S, Lee J, et al. Contrast-enhanced MRI T1 Mapping for Quantitative Evaluation of Putative Dynamic Glymphatic Activity in the Human Brain in Sleep-Wake States. Radiology [Internet]. 2021 [cited 2025 Oct 6];300:661–8. https://doi.org/10.1148/radiol.2021203784

19. Richmond SB, Rane S, Hanson MR, Albayram M, Iliff JJ, Kernagis D, et al. Quantification approaches for magnetic resonance imaging following intravenous gadolinium injection: A window into brain-wide glymphatic function. Eur J of Neuroscience [Internet]. 2023 [cited 2024 Nov 27];57:1689–704. https://doi.org/10.1111/ejn.15974

20. Van Osch MJP, Wåhlin A, Scheyhing P, Mossige I, Hirschler L, Eklund A, et al. Human brain clearance imaging: Pathways taken by magnetic resonance imaging contrast agents after administration in cerebrospinal fluid and blood. NMR in Biomedicine [Internet]. 2024 [cited 2024 Nov 27];37:e5159. https://doi.org/10.1002/nbm.5159

21. Taoka T, Masutani Y, Kawai H, Nakane T, Matsuoka K, Yasuno F, et al. Evaluation of glymphatic system activity with the diffusion MR technique: diffusion tensor image analysis along the perivascular space (DTI-ALPS) in Alzheimer's disease cases. Jpn J Radiol [Internet]. 2017 [cited 2022 Sep 1];35:172–8. https://doi.org/10.1007/s11604-017-0617-z

22. Premi E, Diano M, Mattioli I, Altomare D, Cantoni V, Bocchetta M, et al. Impaired glymphatic system in genetic frontotemporal dementia: a GENFI study. Brain Communications [Internet]. 2024 [cited 2025 Oct 6];6:fcae185. https://doi.org/10.1093/braincomms/fcae185

23. Jiang D, Liu L, Kong Y, Chen Z, Rosa-Neto P, Chen K, et al. Regional Glymphatic Abnormality in Behavioral Variant Frontotemporal Dementia. Annals of Neurology [Internet]. 2023 [cited 2023 Oct 21];94:442–56. https://doi.org/10.1002/ana.26710

24. Xiao D, Li J, Ren Z, Dai M, Jiang Y, Qiu T, et al. Association of cortical morphology, white matter hyperintensity, and glymphatic function in frontotemporal dementia variants. Alzheimer's & Dementia [Internet]. 2024 [cited 2025 Oct 6];20:6045–59. https://doi.org/10.1002/alz.14158

25. Kamagata K, Andica C, Takabayashi K, Saito Y, Taoka T, Nozaki H, et al. Association of MRI Indices of Glymphatic System With Amyloid Deposition and Cognition in Mild Cognitive Impairment and Alzheimer Disease. Neurology [Internet]. 2022 [cited 2023 Jan 14];99:e2648–60. https://doi.org/10.1212/WNL.0000000000201300

26. Sacchi L, D'Agata F, Campisi C, Arcaro M, Carandini T, Örzsik B, et al. A "glympse" into neurodegeneration: Diffusion MRI and cerebrospinal fluid AQUAPORIN-4 for the assessment of glymphatic system in Alzheimer's disease and other dementias. Human Brain Mapping [Internet]. 2024 [cited 2024 Nov 27];45:e26805. https://doi.org/10.1002/hbm.26805

27. Hsu J, Wei Y, Toh CH, Hsiao I, Lin K, Yen T, et al. MAGNETIC RESONANCE Images Implicate That Glymphatic Alterations Mediate Cognitive Dysfunction in ALZHEIMER DISEASE. Annals of Neurology [Internet]. 2023 [cited 2023 Oct 21];93:164–74. https://doi.org/10.1002/ana.26516

28. Huang S, Zhang Y, Guo Y, Du J, Ren P, Wu B, et al. Glymphatic system dysfunction predicts amyloid deposition, neurodegeneration, and clinical progression in Alzheimer's disease. Alzheimer's & Dementia [Internet]. 2024 [cited 2024 May 16];20:3251–69. https://doi.org/10.1002/alz.13789

29. Wood KH, Nenert R, Miften AM, Kent GW, Sleyster M, Memon RA, et al. DIFFUSION TENSOR IMAGING-ALONG THE PERIVASCULAR-SPACE Index Is Associated with Disease Progression in Parkinson's Disease. Movement Disorders [Internet]. 2024 [cited 2025 Oct 6];39:1504–13. https://doi.org/10.1002/mds.29908

30. Gu L, Dai S, Guo T, Si X, Lv D, Wang Z, et al. Noninvasive neuroimaging provides evidence for deterioration of the glymphatic system in Parkinson's disease relative to essential tremor. Parkinsonism & Related Disorders [Internet]. 2023 [cited 2025 Oct 6];107:105254. https://doi.org/10.1016/j.parkreldis.2022.105254

31. Ringstad G. Glymphatic imaging: a critical look at the DTI-ALPS index. Neuroradiology [Internet]. 2024 [cited 2024 May 17];66:157–60. https://doi.org/10.1007/s00234-023-03270-2

32. Taoka T, Ito R, Nakamichi R, Nakane T, Kawai H, Naganawa S. Diffusion Tensor Image Analysis ALong the Perivascular Space (DTI-ALPS): Revisiting the Meaning and Significance of the Method. MRMS [Internet]. 2024 [cited 2024 Nov 27];23:268–90. https://doi.org/10.2463/mrms.rev.2023-0175

33. Schilling KG, Newton A, Tax C, Nilsson M, Chamberland M, Anderson A, et al. White Matter Geometry Confounds Diffusion Tensor Imaging Along Perivascular Space (DTI-ALPS) Measures. Human Brain Mapping [Internet]. 2025 [cited 2025 Oct 5];46:e70282. https://doi.org/10.1002/hbm.70282

34. Georgiopoulos C, Werlin A, Lasic S, Hall S, Van Westen D, Spotorno N, et al. Diffusion tensor imaging along the perivascular space: the bias from crossing fibres. Brain Communications [Internet]. 2024 [cited 2025 Oct 6];6:fcae421. https://doi.org/10.1093/braincomms/fcae421

35. Wright AM, Wu Y, Chen N, Wen Q. Exploring Radial Asymmetry in MR Diffusion Tensor Imaging and Its Impact on the Interpretation of Glymphatic Mechanisms. Magnetic Resonance Imaging [Internet]. 2024 [cited 2024 Nov 27];60:1432–41. https://doi.org/10.1002/jmri.29203

36. Wedeen VJ, Wang RP, Schmahmann JD, Benner T, Tseng WYI, Dai G, et al. Diffusion spectrum magnetic resonance imaging (DSI) tractography of crossing fibers. NeuroImage [Internet]. 2008 [cited 2025 Oct 6];41:1267–77. https://doi.org/10.1016/j.neuroimage.2008.03.036

37. Vos SB, Jones DK, Jeurissen B, Viergever MA, Leemans A. The influence of complex white matter architecture on the mean diffusivity in diffusion tensor MRI of the human brain. NeuroImage [Internet]. 2012 [cited 2025 Oct 5];59:2208–16. https://doi.org/10.1016/j.neuroimage.2011.09.086

38. Bozzali M, Franceschi M, Falini A, Pontesilli S, Cercignani M, Magnani G, et al. Quantification of tissue damage in AD using diffusion tensor and magnetization transfer MRI. Neurology [Internet]. 2001 [cited 2025 Oct 5];57:1135–7. https://doi.org/10.1212/WNL.57.6.1135

39. Agosta F, Pievani M, Sala S, Geroldi C, Galluzzi S, Frisoni GB, et al. White Matter Damage in Alzheimer Disease and Its Relationship to Gray Matter Atrophy. Radiology [Internet]. 2011 [cited 2025 Oct 10];258:853–63. https://doi.org/10.1148/radiol.10101284

40. Chen Y, Wang Y, Song Z, Fan Y, Gao T, Tang X. Abnormal white matter changes in Alzheimer's disease based on diffusion tensor imaging: A systematic review. Ageing Research Reviews [Internet]. 2023 [cited 2025 Oct 5];87:101911. https://doi.org/10.1016/j.arr.2023.101911

41. Stricker NH, Schweinsburg BC, Delano-Wood L, Wierenga CE, Bangen KJ, Haaland KY, et al. Decreased white matter integrity in late-myelinating fiber pathways in Alzheimer's disease supports retrogenesis. NeuroImage [Internet]. 2009 [cited 2025 Oct 5];45:10–6. https://doi.org/10.1016/j.neuroimage.2008.11.027

42. Fornari E, Maeder P, Meuli R, Ghika J, Knyazeva MG. Demyelination of superficial white matter in early Alzheimer's disease: a magnetization transfer imaging study. Neurobiology of Aging [Internet]. 2012 [cited 2025 Oct 5];33:428.e7-428.e19. https://doi.org/10.1016/j.neurobiolaging.2010.11.014

43. Ennis DB, Kindlmann G. Orthogonal tensor invariants and the analysis of diffusion tensor magnetic resonance images. Magnetic Resonance in Med [Internet]. 2006 [cited 2025 Oct 7];55:136–46. https://doi.org/10.1002/mrm.20741

44. Bergamino M, Walsh RR, Stokes AM. Free-water diffusion tensor imaging improves the accuracy and sensitivity of white matter analysis in Alzheimer's disease. Sci Rep [Internet]. 2021 [cited 2023 Oct 21];11:6990. https://doi.org/10.1038/s41598-021-86505-7

45. Jones DK, Cercignani M. Twenty-five pitfalls in the analysis of diffusion MRI data. NMR in Biomedicine [Internet]. 2010 [cited 2023 Oct 21];23:803–20. https://doi.org/10.1002/nbm.1543

46. Zhang H, Schneider T, Wheeler-Kingshott CA, Alexander DC. NODDI: Practical in vivo neurite orientation dispersion and density imaging of the human brain. NeuroImage [Internet]. 2012 [cited 2025 Oct 6];61:1000–16. https://doi.org/10.1016/j.neuroimage.2012.03.072

47. Kamiya K, Hori M, Aoki S. NODDI in clinical research. Journal of Neuroscience Methods [Internet]. 2020 [cited 2025 Oct 5];346:108908. https://doi.org/10.1016/j.jneumeth.2020.108908

48. Raykov PP, Correia M, Tsvetanov K, Henriques RN, Del Cerro-León A, Bracher-Smith M, et al. Complementary MR measures of white matter and their relation to cardiovascular health and cognition. Sci Rep [Internet]. 2025 [cited 2025 Oct 5];15:28890. https://doi.org/10.1038/s41598-025-13610-2

49. Glasser MF, Van Essen DC. Mapping Human Cortical Areas *In Vivo* Based on Myelin Content as Revealed by T1- and T2-Weighted MRI. J Neurosci [Internet]. 2011 [cited 2025 Oct 6];31:11597–616.

https://doi.org/10.1523/JNEUROSCI.2180-11.2011

50. Ganzetti M, Wenderoth N, Mantini D. Whole brain myelin mapping using T1- and T2-weighted MR imaging data. Front Hum Neurosci [Internet]. 2014 [cited 2025 Oct 5];8. https://doi.org/10.3389/fnhum.2014.00671

51. Cappelle S, Pareto D, Sunaert S, Smets I, Laenen A, Dubois B, et al. T1w/FLAIR ratio standardization as a myelin marker in MS patients. NeuroImage: Clinical [Internet]. 2022 [cited 2025 Oct 5];36:103248. https://doi.org/10.1016/j.nicl.2022.103248

52. Lee S-N, Woo S-H, Lee EJ, Kim KK, Kim H-R. Association between T1w/T2w ratio in white matter and cognitive function in Alzheimer's disease. Sci Rep [Internet]. 2024 [cited 2025 Oct 5];14:7228. https://doi.org/10.1038/s41598-024-57287-5

53. Operto G, Molinuevo JL, Cacciaglia R, Falcon C, Brugulat-Serrat A, Suárez-Calvet M, et al. Interactive effect of age and APOE-ε4 allele load on white matter myelin content in cognitively normal middle-aged subjects. NeuroImage: Clinical [Internet]. 2019 [cited 2025 Oct 5];24:101983. https://doi.org/10.1016/j.nicl.2019.101983

54. Acosta-Cabronero J, Williams GB, Cardenas-Blanco A, Arnold RJ, Lupson V, Nestor PJ. In Vivo Quantitative Susceptibility Mapping (QSM) in Alzheimer's Disease. Connor JR, editor. PLoS ONE [Internet]. 2013 [cited 2022 Apr 17];8:e81093. https://doi.org/10.1371/journal.pone.0081093

55. Kiersnowski OC, Mattioli P, Argenti L, Avanzino L, Calizzano F, Diociasi A, et al. Magnetic susceptibility components reveal different aspects of neurodegeneration in alpha-synucleinopathies. Sci Rep [Internet]. 2025 [cited 2025 Oct 6];15:4186. https://doi.org/10.1038/s41598-024-83593-z

56. Ahmed M, Chen J, Arani A, Senjem ML, Cogswell PM, Jack CR, et al. The diamagnetic component map from quantitative susceptibility mapping (QSM) source separation reveals pathological alteration in Alzheimer's disease-driven neurodegeneration. NeuroImage [Internet]. 2023 [cited 2025 Oct 5];280:120357. https://doi.org/10.1016/j.neuroimage.2023.120357

57. Levendovszky SR, Meyer B. Diffusion Tensor Imaging in Neurofluids. Neuroimaging Clinics of North America [Internet]. 2025 [cited 2025 Oct 6];35:211–22. https://doi.org/10.1016/j.nic.2024.11.001

58. Dubois B, Villain N, Frisoni GB, Rabinovici GD, Sabbagh M, Cappa S, et al. Clinical diagnosis of Alzheimer's disease: recommendations of the International Working Group. The Lancet Neurology [Internet]. 2021 [cited 2022 Apr 17];20:484–96. https://doi.org/10.1016/S1474-4422(21)00066-1

59. Jack CR, Bennett DA, Blennow K, Carrillo MC, Dunn B, Haeberlein SB, et al. NIA-AA Research Framework: Toward a biological definition of Alzheimer's disease. Alzheimer's & Dementia [Internet]. 2018 [cited 2021 Mar 13];14:535–62. https://doi.org/10.1016/j.jalz.2018.02.018

60. Rascovsky K, Hodges JR, Knopman D, Mendez MF, Kramer JH, Neuhaus J, et al. Sensitivity of revised diagnostic criteria for the behavioural variant of frontotemporal dementia. Brain [Internet]. 2011 [cited 2022 Sep 1];134:2456–77. https://doi.org/10.1093/brain/awr179

61. Armstrong MJ, Litvan I, Lang AE, Bak TH, Bhatia KP, Borroni B, et al. Criteria for the diagnosis of corticobasal degeneration. Neurology [Internet]. 2013 [cited 2023 Oct 21];80:496–503. https://doi.org/10.1212/WNL.0b013e31827f0fd1

62. McKeith IG, Boeve BF, Dickson DW, Halliday G, Taylor J-P, Weintraub D, et al. Diagnosis and management of dementia with Lewy bodies: Fourth consensus report of the DLB Consortium. Neurology [Internet]. 2017 [cited 2021 Mar 20];89:88–100. https://doi.org/10.1212/WNL.0000000000004058

63. Gorno-Tempini ML, Hillis AE, Weintraub S, Kertesz A, Mendez M, Cappa SF, et al. Classification of primary progressive aphasia and its variants. Neurology [Internet]. 2011 [cited 2021 Mar 20];76:1006–14. https://doi.org/10.1212/WNL.0b013e31821103e6

64. Höglinger GU, Respondek G, Stamelou M, Kurz C, Josephs KA, Lang AE, et al. Clinical diagnosis of progressive supranuclear palsy: The movement disorder society criteria: MDS Clinical Diagnostic Criteria for PSP. Mov Disord [Internet]. 2017 [cited 2023 Oct 25];32:853–64. https://doi.org/10.1002/mds.26987

65. Liu X, Barisano G, Shao X, Jann K, Ringman JM, Lu H, et al. Cross-Vendor Test-Retest Validation of Diffusion Tensor Image Analysis along the Perivascular Space (DTI-ALPS) for Evaluating Glymphatic System

Function. Aging and disease [Internet]. 2023 [cited 2025 Oct 5];0. https://doi.org/10.14336/AD.2023.0321-2

66. Smith SM, Jenkinson M, Woolrich MW, Beckmann CF, Behrens TEJ, Johansen-Berg H, et al. Advances in functional and structural MR image analysis and implementation as FSL. NeuroImage [Internet]. 2004 [cited 2025 Oct 7];23:S208–19. https://doi.org/10.1016/j.neuroimage.2004.07.051

67. Jenkinson M, Beckmann CF, Behrens TEJ, Woolrich MW, Smith SM. FSL. NeuroImage [Internet]. 2012 [cited 2025 Oct 7];62:782–90. https://doi.org/10.1016/j.neuroimage.2011.09.015

68. Andersson JLR, Skare S, Ashburner J. How to correct susceptibility distortions in spin-echo echo-planar images: application to diffusion tensor imaging. NeuroImage [Internet]. 2003 [cited 2025 Oct 7];20:870–88. https://doi.org/10.1016/S1053-8119(03)00336-7

69. Andersson JLR, Sotiropoulos SN. An integrated approach to correction for off-resonance effects and subject movement in diffusion MR imaging. NeuroImage [Internet]. 2016 [cited 2023 Oct 21];125:1063–78. https://doi.org/10.1016/j.neuroimage.2015.10.019

70. Smith SM. Fast robust automated brain extraction. Hum Brain Mapp [Internet]. 2002 [cited 2022 Apr 26];17:143–55. https://doi.org/10.1002/hbm.10062

71. Jenkinson M, Bannister P, Brady M, Smith S. Improved Optimization for the Robust and Accurate Linear Registration and Motion Correction of Brain Images. NeuroImage [Internet]. 2002 [cited 2025 Oct 7];17:825–41. https://doi.org/10.1006/nimg.2002.1132

72. Tustison NJ, Avants BB, Cook PA, Yuanjie Zheng, Egan A, Yushkevich PA, et al. N4ITK: Improved N3 Bias Correction. IEEE Trans Med Imaging [Internet]. 2010 [cited 2023 Oct 21];29:1310–20. https://doi.org/10.1109/TMI.2010.2046908

73. Chen J, Gong N-J, Chaim KT, Otaduy MCG, Liu C. Decompose quantitative susceptibility mapping (QSM) to sub-voxel diamagnetic and paramagnetic components based on gradient-echo MRI data. NeuroImage [Internet]. 2021 [cited 2025 Oct 5];242:118477. https://doi.org/10.1016/j.neuroimage.2021.118477

74. Lancione M, Cencini M, Costagli M, Donatelli G, Tosetti M, Giannini G, et al. Diagnostic accuracy of quantitative susceptibility mapping in multiple system atrophy: The impact of echo time and the potential of histogram analysis. NeuroImage: Clinical [Internet]. 2022 [cited 2025 Oct 7];34:102989. https://doi.org/10.1016/j.nicl.2022.102989

75. Daducci A, Canales-Rodríguez EJ, Zhang H, Dyrby TB, Alexander DC, Thiran J-P. Accelerated Microstructure Imaging via Convex Optimization (AMICO) from diffusion MRI data. NeuroImage [Internet]. 2015 [cited 2025 Oct 7];105:32–44. https://doi.org/10.1016/j.neuroimage.2014.10.026

76. Revelle W. psych: Procedures for Psychological, Psychometric, and Personality Research [Internet]. 2007 [cited 2025 Oct 7]. p. 2.5.6. https://doi.org/10.32614/CRAN.package.psych

77. the EDSD study group, Teipel SJ, Grothe MJ, Filippi M, Fellgiebel A, Dyrba M, et al. Fractional Anisotropy Changes in Alzheimer's Disease Depend on the Underlying Fiber Tract Architecture: A Multiparametric DTI Study using Joint Independent Component Analysis. JAD [Internet]. 2014 [cited 2025 Oct 5];41:69–83. https://doi.org/10.3233/JAD-131829

78. Douaud G, Jbabdi S, Behrens TEJ, Menke RA, Gass A, Monsch AU, et al. DTI measures in crossing-fibre areas: Increased diffusion anisotropy reveals early white matter alteration in MCI and mild Alzheimer's disease. NeuroImage [Internet]. 2011 [cited 2025 Oct 5];55:880–90. https://doi.org/10.1016/j.neuroimage.2010.12.008

79. Mito R, Raffelt D, Dhollander T, Vaughan DN, Tournier J-D, Salvado O, et al. Fibre-specific white matter reductions in Alzheimer's disease and mild cognitive impairment. Brain [Internet]. 2018 [cited 2025 Oct 5];141:888–902. https://doi.org/10.1093/brain/awx355

80. Li S, Chen R, Cao Z, Zhu Q, Ma Y, Zhu K, et al. Microstructural Bias in the Assessment of Periventricular Flow as Revealed in Postmortem Brains. Radiology [Internet]. 2025 [cited 2025 Oct 5];316:e250753. https://doi.org/10.1148/radiol.250753

81. Barisano G, Lynch KM, Sibilia F, Lan H, Shih N-C, Sepehrband F, et al. Imaging perivascular space structure and function using brain MRI. Neuroimage. 2022;257:119329. https://doi.org/10.1016/j.neuroimage.2022.119329

82. Uddin MN, Figley TD, Marrie RA, Figley CR, for the CCOMS Study Group. Can T_1 w/ T_2 w ratio be used as a myelin-specific measure in subcortical structures? Comparisons between FSE-based T_1 w/ T_2 w ratios, GRASE-based T_1 w/ T_2 w ratios and multi-echo GRASE-based myelin water fractions. NMR in Biomedicine [Internet]. 2018 [cited 2025 Oct 6];31:e3868. https://doi.org/10.1002/nbm.3868

83. Arshad M, Stanley JA, Raz N. Test–retest reliability and concurrent validity of in vivo myelin content indices: Myelin water fraction and calibrated T_1 w/T_2 w image ratio. Human Brain Mapping [Internet]. 2017 [cited 2025 Oct 6];38:1780–90. https://doi.org/10.1002/hbm.23481

84. Hagiwara A, Hori M, Kamagata K, Warntjes M, Matsuyoshi D, Nakazawa M, et al. Myelin Measurement: Comparison Between Simultaneous Tissue Relaxometry, Magnetization Transfer Saturation Index, and T1w/T2w Ratio Methods. Sci Rep [Internet]. 2018 [cited 2025 Oct 6];8:10554. https://doi.org/10.1038/s41598-018-28852-6

85. Righart R, Biberacher V, Jonkman LE, Klaver R, Schmidt P, Buck D, et al. Cortical pathology in multiple sclerosis detected by the T 1/ T 2-weighted ratio from routine magnetic resonance imaging. Annals of Neurology [Internet]. 2017 [cited 2025 Oct 6];82:519–29. https://doi.org/10.1002/ana.25020

86. Nakamura M, Iwasaki Y, Takahashi T, Kaneko K, Nakashima I, Kunieda T, et al. A case of MOG antibody-positive bilateral optic neuritis and meningoganglionitis following a genital herpes simplex virus infection. Mult Scler Relat Disord. Netherlands; 2017;17:148–50. https://doi.org/10.1016/j.msard.2017.07.023

87. Sandrone S, Aiello M, Cavaliere C, Thiebaut De Schotten M, Reimann K, Troakes C, et al. Mapping myelin in white matter with T1-weighted/T2-weighted maps: discrepancy with histology and other myelin MRI measures. Brain Struct Funct [Internet]. 2023 [cited 2025 Oct 5];228:525–35. https://doi.org/10.1007/s00429-022-02600-z

88. Uchida Y, Kan H, Sakurai K, Oishi K, Matsukawa N. Quantitative susceptibility mapping as an imaging biomarker for Alzheimer's disease: The expectations and limitations. Front Neurosci [Internet]. 2022 [cited 2025 Oct 5];16:938092. https://doi.org/10.3389/fnins.2022.938092

89. Lancione M, Tosetti M, Donatelli G, Cosottini M, Costagli M. The impact of white matter fiber orientation in single-acquisition quantitative susceptibility mapping. NMR in Biomedicine [Internet]. 2017 [cited 2025 Oct 5];30:e3798. https://doi.org/10.1002/nbm.3798

90. Slattery CF, Zhang J, Paterson RW, Foulkes AJM, Carton A, Macpherson K, et al. ApoE influences regional white-matter axonal density loss in Alzheimer's disease. Neurobiology of Aging [Internet]. 2017 [cited 2025 Oct 5];57:8–17. https://doi.org/10.1016/j.neurobiolaging.2017.04.021

91. Zhang J, Gregory S, Scahill RI, Durr A, Thomas DL, Lehericy S, et al. In vivo characterization of white matter pathology in premanifest huntington's disease. Annals of Neurology [Internet]. 2018 [cited 2025 Oct 5];84:497–504. https://doi.org/10.1002/ana.25309

92. Grussu F, Schneider T, Tur C, Yates RL, Tachrount M, Ianuş A, et al. Neurite dispersion: a new marker of multiple sclerosis spinal cord pathology? Ann Clin Transl Neurol [Internet]. 2017 [cited 2025 Oct 6];4:663–79. https://doi.org/10.1002/acn3.445

93. Schilling KG, Janve V, Gao Y, Stepniewska I, Landman BA, Anderson AW. Histological validation of diffusion MRI fiber orientation distributions and dispersion. NeuroImage [Internet]. 2018 [cited 2025 Oct 6];165:200–21. https://doi.org/10.1016/j.neuroimage.2017.10.046

94. Tariq M, Schneider T, Alexander DC, Gandini Wheeler-Kingshott CA, Zhang H. Bingham–NODDI: Mapping anisotropic orientation dispersion of neurites using diffusion MRI. NeuroImage [Internet]. 2016 [cited 2025 Oct 5];133:207–23. https://doi.org/10.1016/j.neuroimage.2016.01.046

95. Zhang W, Zhou Y, Wang J, Gong X, Chen Z, Zhang X, et al. Glymphatic clearance function in patients with cerebral small vessel disease. NeuroImage [Internet]. 2021 [cited 2023 Oct 21];238:118257. https://doi.org/10.1016/j.neuroimage.2021.118257